



1 **A method for retrieving clouds with satellite infrared**
2 **radiances using the particle filter**

3 Dongmei Xu^{1,2}, Thomas Auligné², Gaël Descombes², and Chris Synder²

4

5 ¹*Collaborative Innovation Center on Forecast and Evaluation of Meteorological*
6 *Disasters, Nanjing University of Information Science & Technology, Nanjing, 210044,*
7 *China*

8 ²*National Center for Atmospheric Research, Boulder, Colorado 80301, USA*

9 (2016/7/2)

10

11

*** Corresponding Author**

Dr. Dongmei Xu

Nanjing University of Information Science & Technology, College of Atmospheric science,

Ningliu road, No. 219, Nanjing, 210044, China

E-mail: xdmjolly@sina.com



12 **Abstract**

13 Ensemble-based techniques have been widely utilized in estimating uncertainties in
14 various problems of interest in geophysical applications. A new cloud retrieval
15 method is proposed based on the efficient Particle Filter (PF) in the framework of
16 Gridpoint Statistical Interpolation system (GSI). The PF cloud retrieval method is
17 compared with the Multivariate and Minimum Residual (MMR) method that was
18 previously established and verified. Cloud retrieval experiments involving a variety of
19 cloudy types are conducted with the PF and MMR methods respectively with
20 measurements of Infrared radiances on multi-sensors onboard both geostationary and
21 polar satellites. It is found that the retrieved cloud masks with both methods are
22 consistent with other independent cloud products. MMR is prone to producing
23 ambiguous small-fraction clouds, while PF detects clearer cloud signals, yielding
24 closer heights of cloud top and cloud base to other references. More collections of
25 small fraction particles are able to effectively estimate the semi-transparent high
26 clouds. It is found that radiances with high spectral resolutions contribute to
27 quantitative cloud top and cloud base retrievals. In addition, a different way of
28 resolving the filtering problem over each model grid is tested to better aggregate the
29 weights with all available sensors considered, which is proven to be less constrained
30 by the ordering of sensors. Compared to the MMR method, the PF method is overall
31 more computationally efficient, and the cost of the model grid-based PF method
32 scales more directly with the number of computing nodes.

33 **Keywords:** cloud retrieval methods, particle filter, GSI system, cloud height



34 1. Introduction

35 Modern polar orbiting and geostationary airborne instruments provide researchers
36 unprecedented opportunities for earth remote sensing with continuous flows and
37 almost complete spectral coverage of data. The primary cloud retrieval products from
38 satellites are cloud mask (CM), cloud height (CH), effective cloud fraction (CF), and
39 vertical structures of clouds with larger temporal and spatial scales. These cloud
40 retrievals provide an immense and valuable combination for better initializing
41 hydrometeors in numerical weather prediction (NWP) (Wu and Smith, 1992;Hu et al.,
42 2006;Bayler et al., 2000;Auligné et al., 2011), regulating the radiation budget for the
43 planet, and understanding the climate feedback mechanism (Rossow and Schiffer,
44 1991;Rossow et al., 1993;Brückner et al., 2014). Advanced cloud retrieval methods
45 are able to retrieve clouds with multispectral techniques (Menzel et al., 1983;Platnick
46 et al., 2003), among which the minimization methods usually directly utilize the
47 difference between the modeled clear sky and the observed cloudy Infrared (IR)
48 radiances (e. g., the minimum residual method, (Eyre and Menzel, 1989) the
49 Minimum Local Emissivity Variance method, (Huang et al., 2004); and the
50 Multivariate Minimum Residual method, (Auligné, 2014a). Specially, the
51 Multivariate Minimum Residual (MMR) method is retrieving three dimensional
52 multi-layer clouds by minimizing a cost function at each field-of-view (FOV)
53 (Auligné, 2014b;Xu et al., 2015). MMR has been proven to be reliable in retrieving
54 the quantitative three dimensional cloud fractions with Infrared radiances from



55 multiple infrared instruments. However, MMR has limitations in several aspects due
56 to its use of minimization for solution: 1) Part of the control variables accounting for
57 the cloud fraction for some certain levels are under-observed since the channels are
58 not sensitive to the existence of clouds for those heights. 2) When clouds at different
59 heights show opacities with the same spectral signal, MMR could lose the ability to
60 distinguish solutions involving clouds at those levels. 3) The computational cost for
61 the minimization procedure in MMR is rather considerable.

62 Ensemble-based techniques, that usually reside in short-term ensemble
63 forecasting (Berrocal et al., 2007), assembling existing model outputs (e. g., cloud
64 retrievals) from varying algorithms (Zhao et al., 2012), or ensemble Kalman filter
65 (EnKF) in various forms (Snyder and Zhang, 2003), have been widely developed in
66 order to estimate the uncertainties of all kinds of problems in geophysical applications.
67 To better account for the non-linearity between the observed radiance and the retrieval
68 parameter, a novel prototype for detecting clouds and retrieving their vertical
69 extension inspired by the particle filter (Snyder et al., 2008;van Leeuwen, 2010;Shen
70 and Tang, 2015) technique and Bayesian theory (Karlsson et al., 2015) is proposed in
71 this study. As a competitive alternative for MMR, the PF retrieval method has same
72 critical inputs required and cloud retrieval products as in MMR. A brief description of
73 MMR and the new PF cloud retrieval algorithm are provided in the following section.
74 Section 3 describes the background model, the data assimilation system, the radiative
75 transfer models (RTMs), and the radiance observations applied in this study. Model
76 configurations are also illustrated in section 3. In section 4, the single test within one



77 FOV is conducted before the performance of PF method is assessed by comparing its
78 cloud retrievals with those from MMR and other operational cloud products. Section 4
79 also discusses the computational performance for the two methods. The conclusion
80 and anticipated future work are outlined in section 5.

81 **2. Methodology**

82 Essentially, the PF cloud retrieval scheme retrieves clouds with the same critical
83 inputs requested (i. e., clear sky radiance from the radiative transfer model and the
84 observed radiance) and the same cloud retrievals as outputs (i. e., effective three
85 dimensional cloud fractions) with the MMR method. Details of the schematic of the
86 MMR method can be referred in (Xu et al., 2015; Descombes et al., 2014). We use
87 $\mathbf{c} = c^1, c^2, \dots, c^K$ to denote the array of vertical effective cloud fractions for K model
88 levels, and c^0 as the fraction of clear sky with $0 \leq c^k \leq 1, \forall k \in [0, K]$. In this study,
89 a cloud on one model level with a given fraction c^k is assumed to block the
90 radiation from its lower model levels. The radiation originating from its lower levels
91 is assumed to contribute to the top of atmosphere radiance observed by the satellites
92 only with the residual fractions. The MMR method is an approach to retrieve cloud
93 fractions using the minimization technique. The residual of the modeled radiance and
94 the observation is normalized by the observed radiance, which results in the following
95 cost function:

$$96 \quad J(\mathbf{c}^0, \mathbf{c}) = \frac{1}{2} \sum_v \left[\frac{R_v^{\text{cloud}} - R_v^{\text{obs}}}{R_v^{\text{obs}}} \right]^2, \quad (1)$$



97 where R_v^{cloud} is the modeled cloudy radiance, and R_v^{obs} the observed radiance at
98 frequency ν . This vertical cloud fraction $\mathbf{c} = c^1, c^2, \dots, c^K$ and c^0 are control variables
99 for the cost function, where the simulated R_v^{cloud} is defined as

$$100 \quad R_v^{\text{cloud}}(c^0, c^1, c^2, \dots, c^K) = c^0 R_v^0 + \sum_{k=1}^K c^k R_v^k, \quad (2)$$

101 with $c^0 + \sum_{k=1}^K c^k = 1$ as the constraint. Here R_v^k is the radiance calculated assuming
102 an overcast black cloud at the model level k and R_v^0 the radiance calculated in the
103 clear sky.

104 While MMR retrieves the cloud fractions on each model vertical level by
105 minimizing a cost function, PF calculates posterior weights for each ensemble
106 member based on the observation likelihood given that member. In its simplest form,
107 PF works by initializing a collection of cloud profiles as particles and then estimating
108 the cloud distributions by averaging those particles with their corresponding weights.
109 Explicitly, each particle's weight is computed with the difference between the
110 modeled cloudy radiance from the particle and the observed radiance.

111 As the probabilities of the cloud distribution are fully presented by the initial
112 particles, of particular interest is to evaluate different particle initialization schemes in
113 the PF method. Two typical approaches for generating particles are firstly designed;
114 the first one is to generate the perturbed samples P_b^i ($\forall i \in [1, n]$) from the cloud
115 profile in the background denoted as $P_b(\mathbf{c} = c^0, c^1, \dots, c^K)$ by inflating, deflating, and
116 moving the clouds with small magnitudes, where n is the sample size. The perturbed
117 cloud fractions are designated to replenish the ensemble by introducing the prior



118 informations of the cloud distributions from the background. Besides those perturbed
 119 particles, to represent the existence of one-layer cloud on each model level with an
 120 even chance, another diversity set of profiles P_b^i ($\forall i \in [1, K + 1]$) are also initialized,
 121 among which, P^i stands for the profile with 100% cloud fraction on the model level i
 122 ($c^i=100\%$) and 0% cloud on the rest levels. In particular, P^0 defines 100% clear ($c^0=1$).
 123 It is also interesting to discretize the initial particles by setting the one-layer cloud
 124 with the value of c^i from 100% to 0% (e. g., 100%, 90%, 80%, ..., 0% with 10% as
 125 the interval) and further from 100% to 0% (e. g., 100%, 99%, 98%, 97%, ..., 0% with
 126 1% as the interval). For each particle P_b^i , its simulated cloudy radiance $R_{v,i}^{\text{cloud}}$ from the
 127 model background can be obtained with Eq. (2). The weight w^i for each particle P_b^i
 128 thus is calculated by comparing the simulated $R_{v,i}^{\text{cloud}}$ and the observation R_v^{obs} using
 129 the exponential function as

$$w^i = e^{-\frac{(R_v^{\text{obs}} - R_{v,i}^{\text{cloud}})^2}{\sigma}}, \quad (3)$$

131 $\forall i \in [1, p]$. Here p is the particle size and σ is the specified observation error. The
 132 final analyzed P_a is obtained by averaging the background particles P_b^i with their
 133 corresponding weight, as

$$P_a(c^0, c^1, c^2, \dots, c^K) = \sum_{i=1}^p w^i P_b^i. \quad (4)$$

135 After updating all the particles, the final averaged cloud fractions c_a^k are
 136 normalized by

$$c_a^k = \frac{c^k}{\sum_{k=0}^K c^k}, \quad (5)$$



138 where $\forall k \in [0, K]$.

139 **3. Data and model configurations**

140 3.1 Data

141 The Advanced Infrared Sounder (AIRS), the Infrared Atmospheric Sounding
142 Interferometer (IASI), and the Cross-track Infrared Sounder (CrIs) are among the
143 most advanced hyperspectral infrared sounders and thus are applied for retrieving
144 clouds with hundreds of channels (Blumstein et al., 2004; Aumann et al., 2003; Xu et
145 al., 2013; Smith et al., 2015). The Radiance measurements from Moderate Resolution
146 Imaging Spectroradiometer (MODIS) onboard the Earth Observing System (EOS)
147 Terra or Aqua satellites are also well suited to extracting valuable cloud information
148 from the 36 spectral broadbands in the visible, near infrared and infrared regions at
149 high spatial resolution (1–5 km) (Ackerman, 1998). Apart from the IR radiances
150 from polar satellites, the Geostationary Operational Environmental Satellites (GOES)
151 Imager (Menzel and Purdom, 1994) provides a continuous stream of data over the
152 observing domain. In this study, GOES-13 (east) and GOES-15 (west) are utilized to
153 obtain cloud fractions over the continental United States (CONUS) domain. The
154 GOES Imager used in this study is a five-channel (one visible, four infrared)
155 imaging radiometer designed to sense radiant and solar reflected energy. The
156 instrument parameters for the sensors and the setups for channel selections can be
157 found in (Xu et al., 2015).



158 3.2 WRF, GSI and the radiative transfer model

159 The background fields are processed running the Weather Research and Forecast
160 (WRF) model (Skamarock et al., 2008). The MMR and PF cloud retrieval algorithms
161 are both implemented based on the gridpoint statistical interpolation data assimilation
162 system (GSI) (Wu et al., 2002; Kleist et al., 2009), which is a widely used data
163 assimilation system in operations and researches in NWP. GSI is capable of ingesting
164 a large variety of satellite radiance observations and has developed capabilities for
165 data thinning, quality control, and satellite radiance bias correction. The Community
166 Radiative Transfer Model (Liu and Weng, 2006; Han et al., 2006) was used as the
167 radiance forward operator for computing the clear-sky radiance and the radiance given
168 overcast clouds at each model level.

169 3.3 Model configurations

170 The WRF is configured with 415*325 horizontal grids at 15-km grid spacing, and
171 40 vertical levels up to 50 hPa within the single CONUS domain. The MMR and PF
172 cloud detection schemes search the cloud top using approximately 150 hPa as the
173 highest extent. Channels in the longwave region are utilized following the channel
174 selection scheme in (Xu et al., 2015). Generally, for each FOV, the retrieved cloud
175 fractions are extrapolated to its four neighboring model grid points. For polar satellite
176 pixels, the representative cloud fractions are extrapolated with an adaptive radius with
177 respect to their scan positions. The cloud detecting procedure for retrieving clouds is
178 conducted for each FOV from each individual sensor independently and sequentially.



179 **4. Experiments and results**

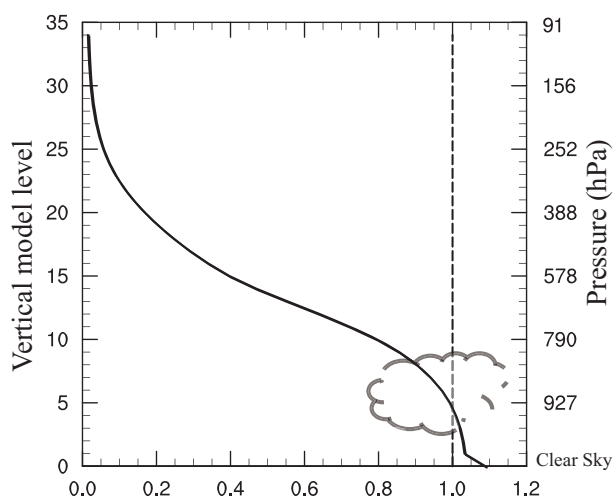
180 The PF experiments apply two groups of particles as mentioned in section 2,
181 among which the group-2 particles contains solely 100% one-layer clouds. To reveal
182 how the setup of the initial particles impacts the results, apart from the MMR and PF
183 experiments, we included another advanced experiment, denoted as APF. APF
184 requires more sampled particles including ranges of cloud fractions spanning from 0%
185 to 100% at the interval of 10%. An additional experiment “APFg2”, similar to APF
186 but excluding the perturbed particles from the background in group-1 introduced in
187 section 2, was conducted to evaluate the added values from the group-one particles. In
188 this section, cloud retrieval experiments for several cases containing clouds of a
189 variety of types are conducted for comparison reason. The GOES imager retrieved
190 products from National Aeronautics and Space Administration (NASA-Langley cloud
191 and radiation products) are applied as a reference to validate the cloud retrieving
192 methods for the CONUS domain with a large and uniform coverage of cloud mask. In
193 addition, the retrieved cloud products were also compared to available CloudSat
194 (Stephens et al., 2002) and MODIS level-2 cloud products (Platnick et al., 2003)
195 archived by the CloudSat Data Processing Center in Colorado State and NASA
196 respectively.

197 4.1 Single test at one field of view

198 The PF cloud retrieving algorithm retrieves the cloud distributions by averaging
199 those initial particles with their weights. Before the real case experiments are carried



200 out over the whole domain, we conduct a single cloud retrieving test at one FOV to
201 understand what differences can be explained by the differences in the basic initial
202 particles. In Eq. (7), the observation error σ can be set proportional to the
203 observation, equaling to $\frac{R_v^{obs}}{o_f}$, where o_f is the prescribed ratio. Thus, the cloud
204 signals on each level k are virtually determined by the extent of how close the $\frac{R_v^k}{R_v^{obs}}$
205 (and $\frac{R_v^0}{R_v^{obs}}$ for the clear part) gets to 1. An example of the ratio of the overcast
206 radiance and the observed radiance $\frac{R_v^k}{R_v^{obs}}$ for each model level is given in Fig. 1 of
207 GOES-Imager for the channel 5 ($\sim 13.00 \mu m$). The clear sky radiance normalized by
208 the observed radiance $\frac{R_v^0}{R_v^{obs}}$ is also shown at the level 0 (Fig. 1). It is expected that
209 the overcast radiance from the RTM decrease with the rising of the altitude. The cloud
210 signal is strongest around level 5, where R_v^k fits R_v^{obs} most closely. The cloud
211 retrievals depend not only on the basic input profiles (i.e., the overcast radiance on
212 each level from RTM normalized by the observed radiance and the clear sky radiance
213 from RTM normalized by the observed radiance) and but also on the algorithm
214 applied for resolving the problem (e.g., MMR and PF in this study).
215



216

217 **Figure 1.** Ratio of the overcast radiances versus the observed radiance starting from the level 1.

218 The ratio of the clear sky radiance normalized by the observed radiance corresponds to the level 0

219 (see text for explanation) for GOES-Imager for the channel 5. The approximate pressures

220 corresponding to the model levels are also denoted.

221 To reveal the roles of various initial particles, Fig. 2a shows the weights for
222 different particles with specified value of cloud fractions (on the x-axis) on specified
223 model levels (on the y-axis) from 10% to 100% every 10% on the given FOV for
224 channel 5 of GOES-Imager for the case shown in Fig. 1. It seems that clouds can be
225 described by particles with both large fractions and small fractions. Low clouds are
226 easily estimated by one-layer cloud profile with large fractions (larger than 10%). The
227 particles with small-fraction high clouds gain some weights to retrieve high clouds.
228 The particle with the one-layer cloud on level 13 seems to gain least weight compared
229 to the others levels. The weights for the particles with cloud fractions from 0% to
230 100% at the interval of 1% are also presented in Fig. 2b. By including more
231 small-fraction one-layer clouds, the clouds around level 13 can be reproduced by the



232 group of refined particles with 1% as the interval for approximate 10% cloud fractions.

233 However, changing the level of the cloud for the fixed fraction (10%) does not seem

234 to change the outgoing radiance much, probably due to the channel's low weight

235 function peak (~750hPa).

236 The normalized J_o for different levels with a specific cloud fraction from 0% to

237 100% every 10% are shown in the bottom panel of Fig. 2, with 10% and 1% as the

238 intervals in Fig. 2c and Fig. 2d respectively. From Fig. 2c, it is found that J_o is

239 smallest around level-5 with 100% cloud fraction (denoted as 1 in legend) for the thin

240 black line, with respect to the fact that the overcast radiance fits the observed radiance

241 most closely for level-5 approximately. The grey line with 10% cloud fraction (0.1 in

242 the legend) corresponds to the existence of a weight peak on level 19 in Fig. 2a. In

243 addition, the gap between the grey line with 0.1 and the other lines from 0.2 to 1

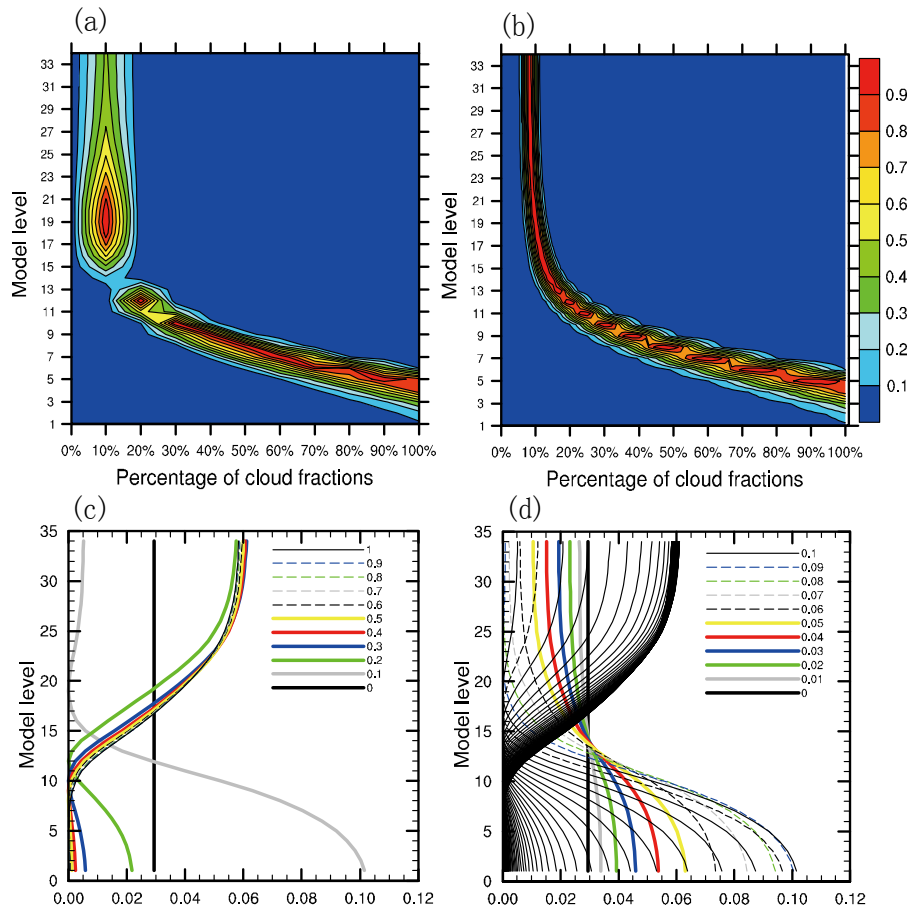
244 explains why there's less continuity around level 13. Fig. 2d shows a similar pattern to

245 Fig. 2c, except with densely-distributed J_o values around the level 13 from 0.1 to 1 in

246 the legend. Those contiguous black lines in Fig. 2d are associated with the set of

247 particles with cloud fractions from 10% to 100% at the interval of 1%.

248



249

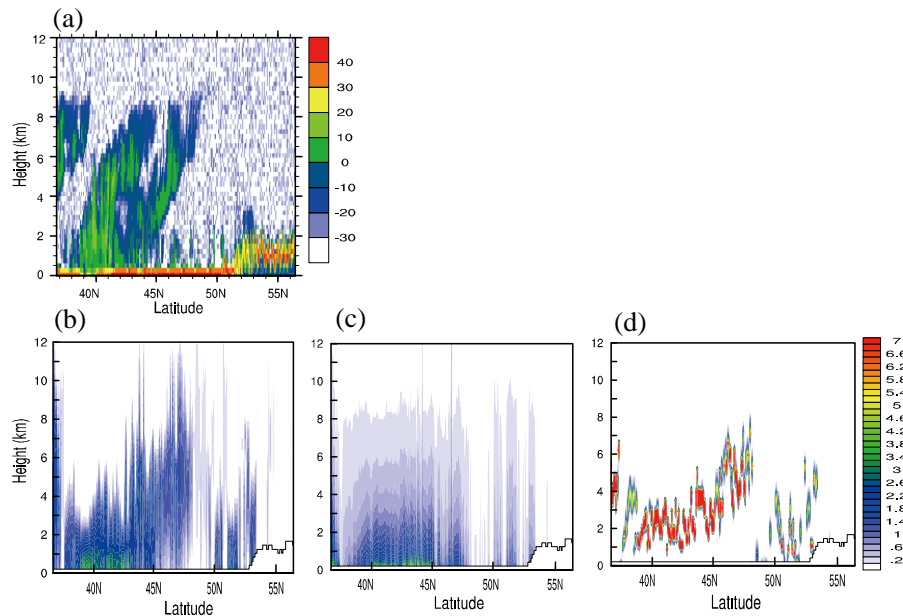
250 **Figure 2.** The weights for different particles with specified cloud fractions on the x-axis at one
 251 chosen model level shown on the y-axis from 0% to 100% (a) at the interval of 10% and (b) at the
 252 interval of 1%. The normalized J_o (c) at the interval of 10% and (d) at the interval of 1%. In (d),
 253 the normalized J_o from 0.1 to 1 are all denoted as black lines.

254 4.2 Cloud profiles

255 The retrieval experiments for a real case are conducted at 1100 UTC 3 June 2012
 256 when AIRS measurements and the CloudSat “2B-GEOPROF” products (Mace, 2004)
 257 are available. The vertical cross sections of the cloud fraction field of a real case are



258 illustrated to further check how different collections of initial particles impact the
259 retrieved cloud profiles. The standard radar reflectivity profiles from the CloudSat are
260 shown in Fig. 3a as the validation source; Fig. 3b, Fig. 3c, and Fig. 3d show the cross
261 sections of the cloud fractions along the CloudSat orbit tracks from the MMR, PF and
262 APF experiments. The vertical structures of the clouds from MMR compare well with
263 the radar reflectivity from CloudSat by retrieving the high clouds around 47N° and
264 low clouds around 52N°. The PF experiment has difficulties in detecting the cloud
265 tops appropriately. PF tends to detect a large quantity of low clouds; by adding a set of
266 particles with small-fraction clouds in APF, higher clouds can be reproduced, which is
267 consistent with the implications from Fig. 2b and 2d. APF detects clear strong cloud
268 signals and removes the cloud fractions on near-surface levels around 36 N°
269 successfully. Since the existences of ground-layer radar reflectivity are likely
270 corresponding to the strong reflection from the underlying surface of the earth, the
271 height of cloud bases of MMR and PF are not compared in this sub-section. The
272 experiments with larger size of particles including 0% to 20% (at the interval of 1%)
273 plus 30% to 100% (at the interval of 10%) or of 0% to 100% (at the interval of 1%)
274 one-layer cloud profiles (introduced in section 2) yield similar results from APF but
275 are much more costly (not shown).



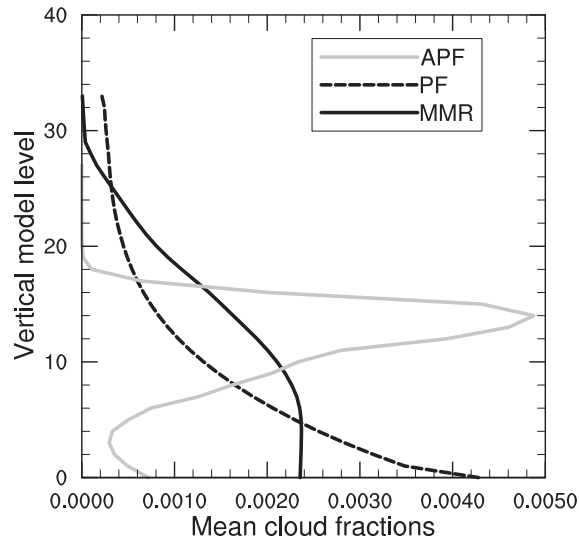
276

277 **Figure 3.** (a) The radar reflectivity (units: DBZ) cross sections from CloudSat, (b) the MMR
278 retrieved cloud fractions (units: %) cross sections, (c) the PF retrieved cloud fractions, and (d) the
279 APF retrieved cloud fractions valid at 1100 UTC 3 June 2012.

280 The vertical profiles of the averaged cloud fractions from MMR, PF, and APF are
281 plotted in Fig. 4 at 1100 UTC 3 June 2012 with AIRS. Both MMR and PF
282 experiments yield ambiguous cloud distributions, whereas APF retrieves much
283 stronger cloud signals constrained between level-2 to level-20 (approximately from
284 950hPa to 400hPa). More clouds around level 10 are retrieved (approximately 750hPa)
285 in MMR, while PF is prone to retrieving clouds near surface levels. Note that MMR
286 retrieves much higher cloud tops and lower cloud bases compared to APF. The cloud
287 base from PF is lowest; the cloud top from MMR and PF is comparable. Only the
288 APF related methods will be further discussed in later sections owing to the missing
289 of high clouds using PF.



290



291

292 **Figure 4.** The mean cloud fraction on all model levels for the experiments MMR, PF, and APF
293 from AIRS valid at 1100 UTC 3 June 2012.

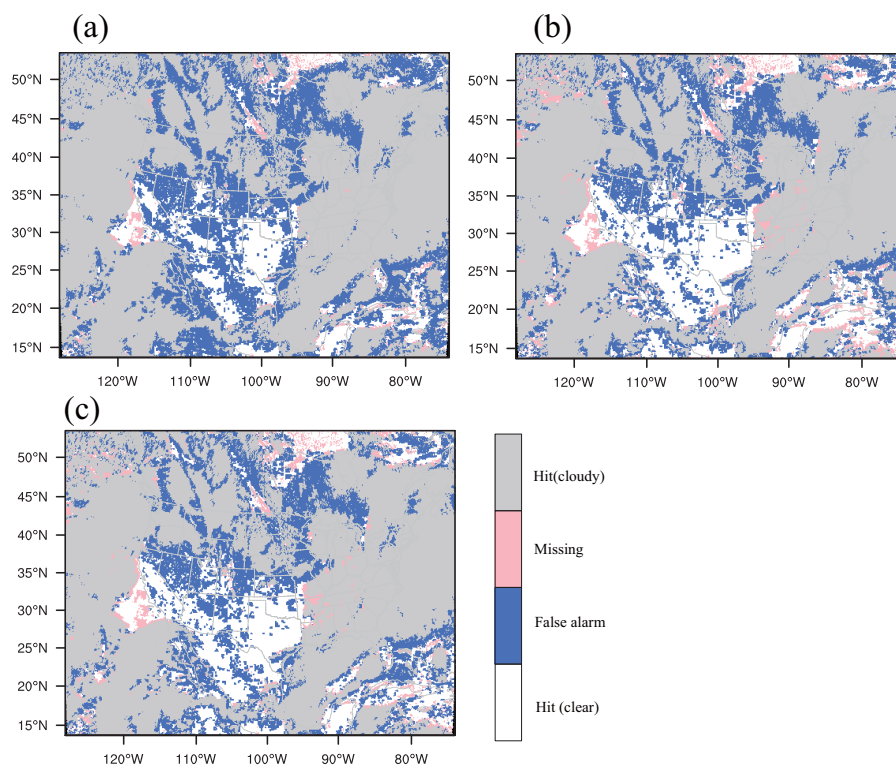
294 4.3 Cloud mask

295 Comparison experiments on real cases are further performed for over longer time
296 period from 0000 UTC 12 December 2013 to 0700 UTC 12 December 2013. The
297 cloud mask is marked as cloudy when there is a recognizable existence of cloud on
298 any level from MMR or PF retrievals. Both the NASA GOES Imager products and the
299 MMR-retrieved fields are interpolated to the same $0.1^\circ \times 0.1^\circ$ latitude–longitude grid
300 with 0 for clear and 1 for cloudy before the comparisons for verification. Fig. 5 shows
301 the *hits*, *false_alarms* and *misses* locations with the use of radiances from
302 GOES-Imager, MODIS, CrIS, AIRS, and IASI in the retrieval algorithms at 0700
303 UTC 12 December 2013. Note that, cloud mask retrievals from both the MMR and
304 APF hit the clear and cloudy events well in Fig. 5a and 5b. In most areas, the MMR



305 experiment overestimated the cloud mask with more false alarm events compared to
306 the APF experiment, since the MMR solution is an “overly smoothed” estimation of
307 the true vertical profile. It seems that the accuracy of cloud detection is lower for
308 areas with high altitude than under tropical conditions, indicating that the smaller
309 lapse rate in the atmosphere will lead radiance less sensitivity to clouds over polar
310 areas. Fig. 5c shows the cloud mask results from the APFg2 experiment without the
311 perturbed particles in group-1 introduced in section 2. There is no large discrepancy
312 between Fig. 5b and Fig. 5c, suggesting that the particles in group-2 that fully span
313 the possibility of the cloud distributions, are more determinant in retrieving the cloud
314 mask.

315



316

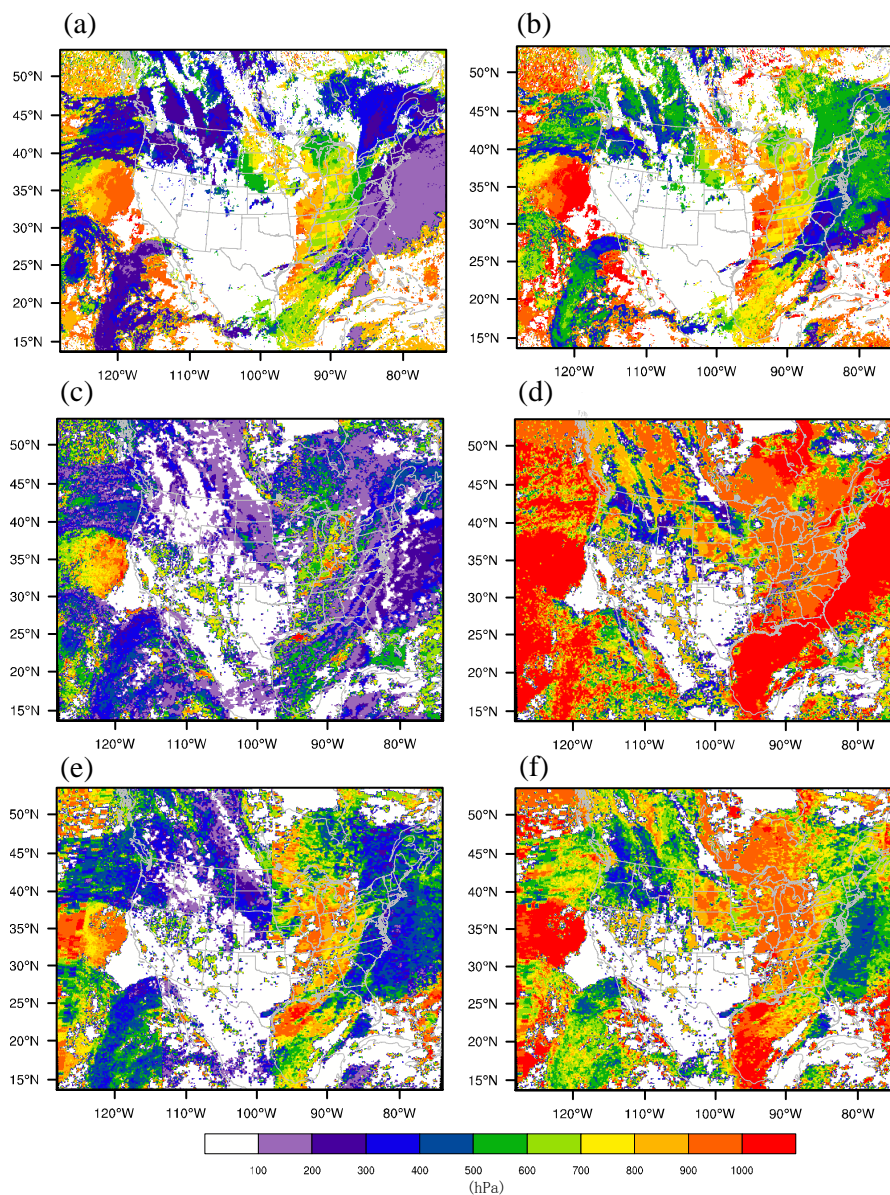


317 **Figure 5.** The false alarms, misses, and hits for clear and cloudy event locations with (a) the MMR
318 method, (b) the APF method, and (c) the APF method but without the group-1 particles (see text
319 for detailed explanations) valid at 0700 UTC 15 December 2013.

320 4.4 Cloud top and base pressure

321 The retrieved cloud top pressures (CTP) and cloud bottom pressures (CBP) from
322 this study along with the NASA GOES cloud products are illustrated in Fig. 6. The
323 CTPs from both methods are in good accordance with the NASA cloud products for
324 high clouds (from 100 hPa to 600 hPa) in Fig. 6a, 6c, and 6e. The retrieved cloud top
325 heights from MMR are overall higher than those from the NASA reference, especially
326 for lower clouds at approximately 750-1000 hPa (e. g., between longitude -100° and
327 -90°). On the other hand, the CTPs from APF are much closer to those in the
328 reference for both high and low clouds. APF overestimates the CBPs for some low
329 clouds (putting the clouds too low) in Fig. 6f; the overestimation of the CBP is even
330 more obvious from MMR in most regions in Fig. 6d.

331



332

333

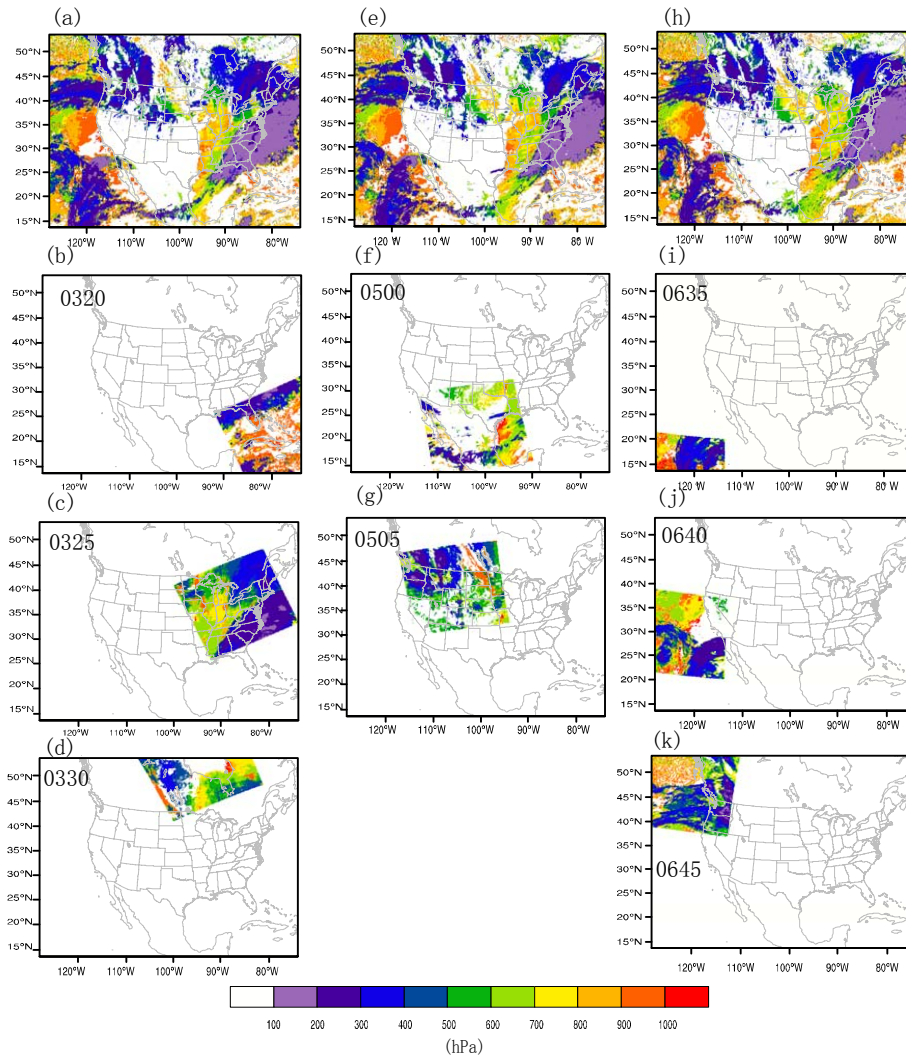
334

335

Figure 6. The cloud top pressure (left panels) from (a) the NASA GOES retrieval, (c) the MMR method, (e) the APF method, and the cloud bottom pressure (right panels) from (b) the NASA GOES retrieval, (d) the MMR method, (f) the APF method valid at 0700 UTC 15 December 2013.



336 The CTPs from NASA GOES cloud products for more hours (0300UTC,
337 0500UTC, 0700UTC) together with the independent CTP retrievals from MODIS
338 level-2 products (http://modis-atmos.gsfc.nasa.gov/MOD06_L2/) are plotted in Fig. 7.
339 Different sub-periods of the MODIS cloud retrieval products (e.g., Fig. 7b valid at
340 0320 UTC, Fig. 7c at 0325, and Fig. 7d at 0330 UTC) are chosen to approach the
341 valid times in Fig. 7a, Fig. 7e, and Fig. 7h respectively. The CTPs from both cloud
342 products agree well for both high and low clouds, confirming that NASA GOES cloud
343 products are overall reliable for verifying the cloud retrievals and MODIS level-2
344 products can also be applied for validations.



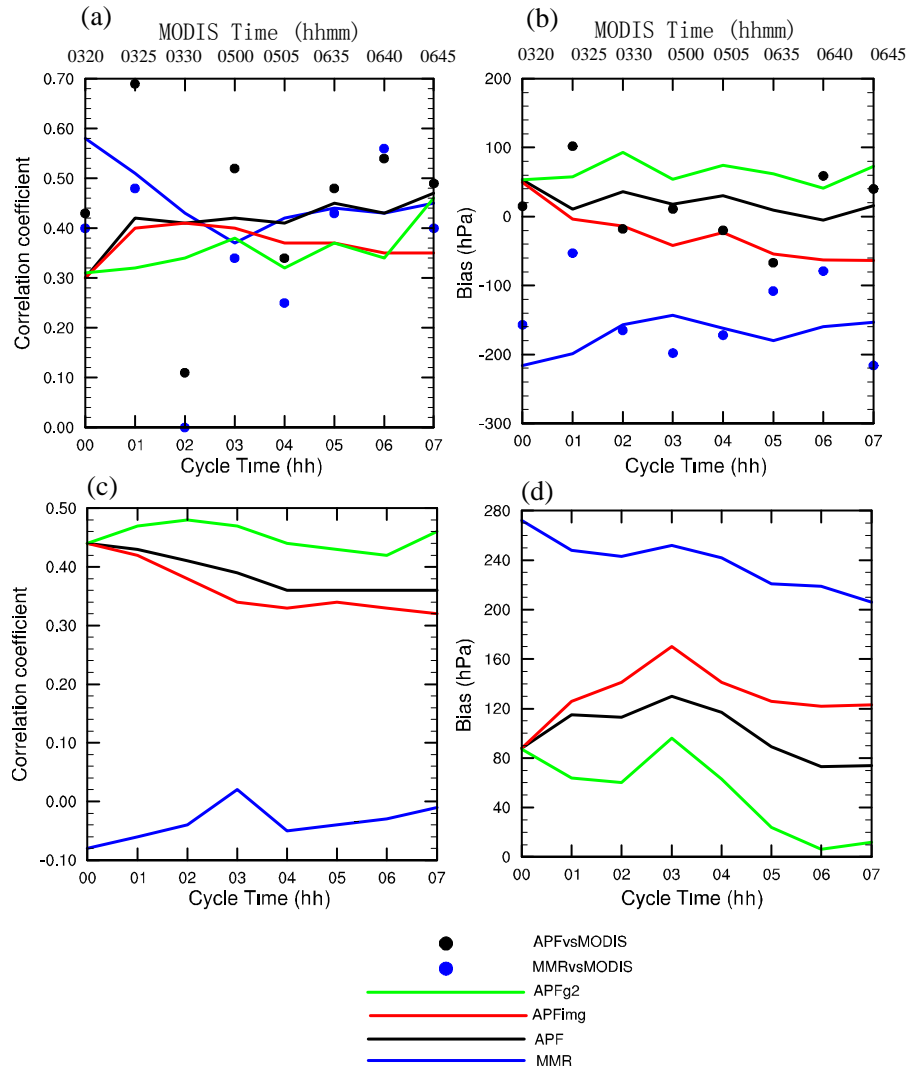
345

346 **Figure 7.** The cloud top pressure for (a) 0300UTC from the GOES NASA retrieval, (b) 0320UTC,
 347 (c) 0325UTC, (d) 0330UTC from MODIS level-2 products; (e) 0500UTC from the GOES NASA
 348 retrieval, (f) 0500UTC, (g) 0505UTC; (h) 0700UTC from the GOES NASA retrieval, (i)
 349 0635UTC, (j) 0640UTC, and (k) 0645UTC from MODIS level-2 products.

350 Fig. 8 presents the correlation coefficients and biases of the CTP and CBP verified
 351 against the NASA GOES and MODIS retrievals. The solid lines denote the results



352 regarding the CTP and CBP versus the NASA GOES products from 0000 UTC to
353 0700 UTC, while the dots describe the CTP results versus the cloud top retrievals in
354 NASA MODIS level-2 products at 0320UTC, 0325UTC, 0330UTC, 0500UTC,
355 0505UTC, 0635UTC, 0640UTC, and 0645UTC. Here the negative bias means that the
356 retrieved clouds are higher than the reference. Vice versa, the positive bias indicates
357 the clouds are put too low. We conducted another experiment “APFimg” that applies
358 solely GOES Imager data to check the added value from the high spectral resolution
359 radiances (such as, CrIS, AIRS, and IASI). In Fig. 8a, the correlations between the
360 retrievals from MMR and the NASA GOES retrievals are comparable with from APF
361 for most hours; APF gains overall higher correlations with the CTPs in the MODIS
362 retrievals. From the bias in Fig. 8b, it seems that the CTPs from MMR are
363 underestimated (putting the clouds too high) consistently against both retrievals from
364 GOES and MODIS. Fig. 8c shows that the correlations are weaker for MMR
365 compared to others all the time. In Fig. 8d, the positive CBP biases from MMR are
366 remarkable, while the CBP biases from APF are largely reduced. Generally, APFimg
367 degrades the CTP and CBP results consistently, suggesting that radiances with high
368 spectral resolutions are able to improve the vertical descriptions of cloud profiles. It is
369 found that the clouds retrieved with APFg2 are shrunken in terms of cloud depth with
370 notably lower cloud top and higher cloud base compared to APF, when excluding the
371 perturbed particles in the first group.



372

373 **Figure 8.** (a) Correlation coefficient, (b) bias for the cloud top pressure, (c) correlation coefficient,

374 and (d) bias for the cloud bottom pressure versus the NASA GOES retrievals from 0600 UTC 15

375 December 2013 to 0700 UTC 15 December 2013. Black and blue dots denote results versus the

376 MODIS level-2 cloud top pressure retrieval valid at 0320UTC, 0325UTC, 0330UTC, 0500UTC,

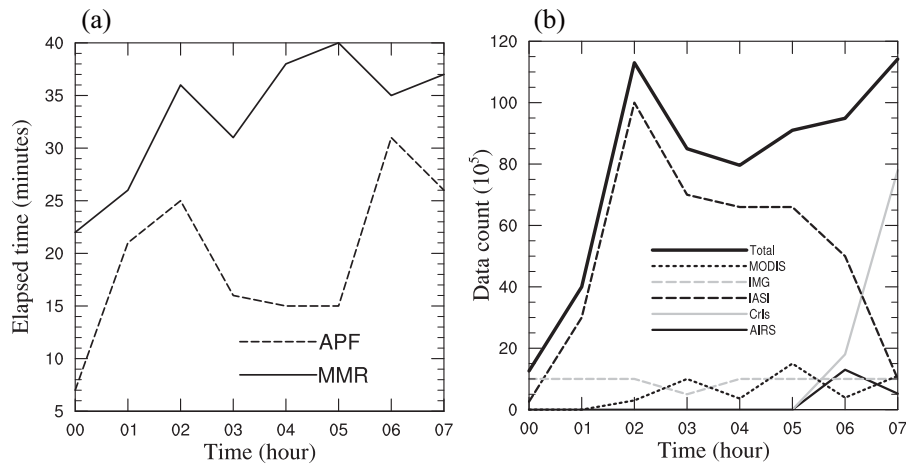
377 0505UTC, 0635UTC, 0640UTC, and 0645UTC. The valid times for the MODIS level-2 data are

378 shown on the top of the x-axis.



379 4.5 Computational issues

380 Fig. 9a represents the elapsed times for the MMR and APF experiments and the
381 counts of radiance observations in use are shown in Fig.9b from 0000 UTC to 0700
382 UTC 12 December 2013. The profile of computing time in MMR is quite different
383 from that in PF. The cost of MMR is dominated by the heavy minimization procedure,
384 while APF is more associated with the processes of initializing particles and
385 calculating weights for all the particles. The computing times were measured from
386 cloud retrieving runs with 64 MPI-tasks on a single computing node in an IBM
387 iDataPlex Cluster. The measured wall clock computing times show that generally
388 MMR is computationally more expensive for most of the time than APF. It seems the
389 wall clock times for MMR are generally proportional to the data amount used. While
390 for the APF experiment, the wall clock time is mostly determined by the particles size
391 and partly affected by the channel number, such as for 2013121202 and 2013121206,
392 when the total counts of the hyperspectral sensors (IASI, CrIs, and AIRS) are large.
393 The PF experiments using particles of one-layer cloud with 100% cloud fractions
394 usually take less than 5 minutes for the same periods (not shown).



395
396 **Figure 9.** (a) The elapsed time and (b) the data count from 0000 UTC to 0700 UTC 15 December
397 2013.

398 4.6 Resolving the filtering problem on model grids

399 As explained in subsection 3.3, the filtering problem is resolved in the radiance
400 observational space at each FOV of each sensor independently and sequentially. For
401 each FOV, the retrieved cloud fractions are extrapolated to its neighboring model grid
402 points afterwards. We order the sensors in the cloud retrieving procedure as
403 GOES-Imager, MODIS, CrIS, AIRS, and IASI, aiming to optimize the vertical clouds
404 using sensors featured with sufficient spectral resolutions. As a consequence, the
405 retrievals from the last sensor determine the final output to the most extent, causing
406 the cloud retrievals highly subjective to the ordering of the sensors. On the other hand,
407 it means the information from other prior sensors will be more or less discarded. In
408 this section, a different way of resolving the filtering problem is preliminarily tested,
409 in which the weights for each particle are aggregated over all available sensors by



410 calling the forward radiative transfer model on neighbouring model grids.

411 Fig. 10 shows the clouds retrievals from the grid-based method. It is noted that

412 the grid-based scheme yields slightly worse results of CTP and neutral results of CBP

413 compared with those from the observation-based (FOV-based) scheme, indicating that

414 the hyperspectral sensors probably favor the retrieved CTP and CBP in the

415 FOV-based scheme, which are available for most of the time. It is worth pointing out

416 that the ordering of different sensors has nearly no effect on the final cloud retrievals,

417 when the weights of the particles are calculated in model space (not shown). The final

418 cloud retrieval is no longer overwritten by the retrieval from the last sensor but is a

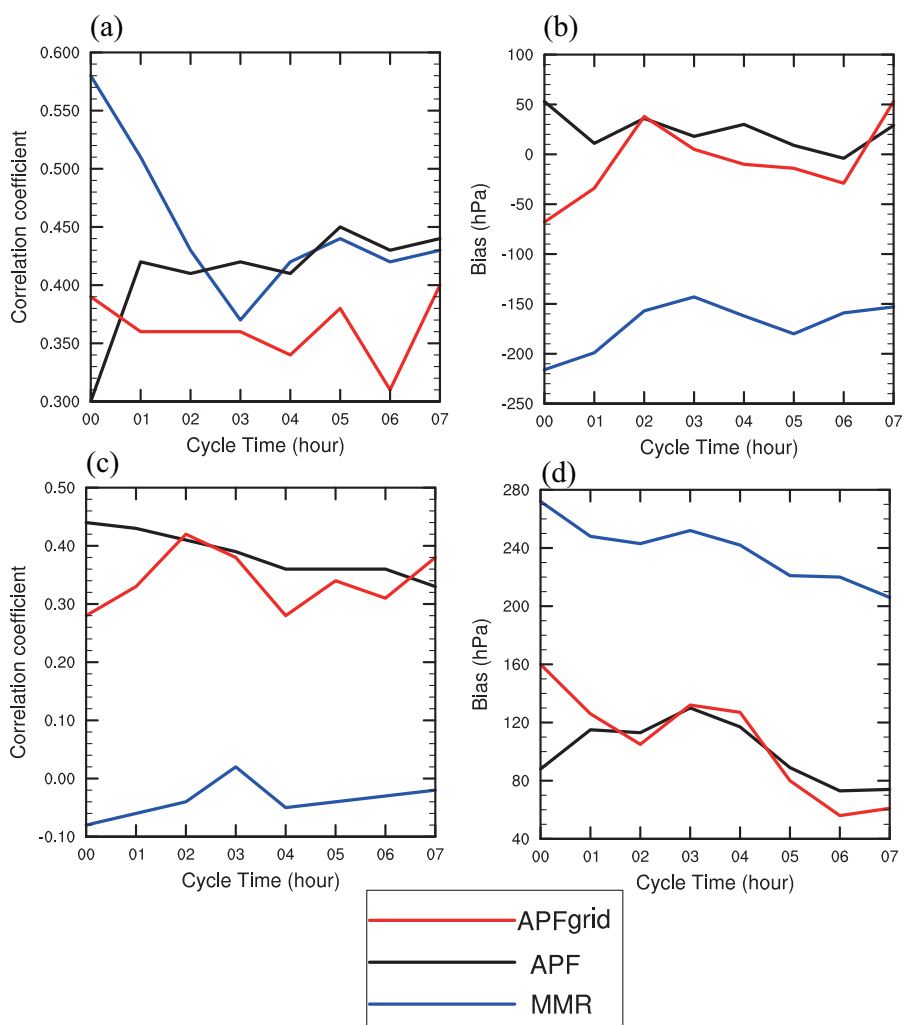
419 total solution with all the sensors fairly considered, instead. The computational cost of

420 retrieving clouds in model space is comparable or slightly heavier than that in

421 observation space. The computational cost of the grid-based scheme scales with the

422 number of the computing nodes more directly, compared to that of the FOV-based

423 scheme.





425 **Figure 10.** (a) Correlation coefficient, (b) bias for the cloud top pressure, (c) correlation
426 coefficient, and (d) bias for the cloud bottom pressure versus the NASA GOES retrievals from
427 0000 UTC to 0700 UTC 15 December 2013.

428 **5. Discussion and conclusion**

429 This study presents a new cloud retrieval method based on the particle filter (PF)
430 in the framework of GSI, as a competitive alternative to the MMR method. The
431 behaviors of different particle initializations are demonstrated on one single field of
432 view and the CONUS domain respectively. Comparisons between the PF and the
433 MMR method are conducted in terms of the features of cloud mask, cloud top, cloud
434 base, and the vertical distributions of clouds. It was found that the PF method
435 retrieves clear cloud signals while MMR is more ambiguous in detecting clouds. By
436 adding more small-fraction particles, high clouds can be better interpreted. From the
437 statistical results, it was found that MMR underestimates the cloud top pressures (put
438 the clouds top too high) and overestimates the cloud bottom pressures (put the clouds
439 top too low) as well. APF improves both the retrievals of cloud tops and cloud bases
440 remarkably, especially for the cloud bases. As expected, radiances with high spectral
441 resolutions contribute to quantitative cloud top and cloud base retrievals. In addition,
442 a different way of resolving the filtering problem over each model grid is tested to
443 aggregate the weights with all available sensors considered, which is proven to be less
444 constrained by the ordering of sensors. Last but not least, the PF method is overall



445 more computationally efficient; the cost of the model grid-based PF method scales
446 more directly with the number of the computing nodes.

447 In future work, validation studies using multispectral imagers on geostationary
448 satellites, spaceborne lidars (or radar), and surface site data will continue, and the
449 results will be used to update the retrieval algorithm. Maximizing the consistency in
450 the products across platforms and optimizing the synergistic use of multiple-source
451 radiances in the new algorithm are important aspects. To estimate the flow dependent
452 uncertainties in the cloud analysis and in the forecasts, the ensemble nowcasting with
453 three dimensional cloud fractions via the rapid-update cycling mode is also planned.
454 Finally, the use of cloud liquid water and ice mixing ratios retrieved from the cloud
455 fractions using multi-sensor radiances to pre-process the first guess in numerical
456 weather forecast is another promising application.

457 **Code and/or data availability**

458 The MMR cloud retrieval codes can be obtained freely from
459 (<http://www2.mmm.ucar.edu/wrf/users/wrfda/>). The other codes can be obtained by emails from
460 the authors.

461



462

REFERENCES

- 463 Ackerman, S. A., K. I. Strabala, W. P. Menzel, R. A. Frey, C. C. Moeller, and L. E.
 464 Gumley: Discriminating clear sky from clouds with MODIS, *Geophys. Res.*
 465 *Atmos.*, 103, 32141-32157, 1998.
- 466 Auligné, T., Lorenc, A., Michel, Y., Montmerle, T., Jones, A., Hu, M., and Dudhia, J.:
 467 Toward a New Cloud Analysis and Prediction System, *B Am Meteorol Soc*, 92,
 468 207-210, 2011.
- 469 Auligné, T.: Multivariate minimum residual method for cloud retrieval. Part I:
 470 Theoretical aspects and simulated observation experiments, *Monthly Weather*
 471 *Review*, 142, 4383-4398, 2014a.
- 472 Auligné, T.: Multivariate minimum residual method for cloud retrieval. Part II: Real
 473 observations experiments, *Monthly Weather Review*, 142, 4399-4415, 2014b.
- 474 Aumann, H. H., Chahine, M. T., Gautier, C., Goldberg, M. D., Kalnay, E., McMillin,
 475 L. M., Revercomb, H., Rosenkranz, P. W., Smith, W. L., and Staelin, D. H.:
 476 AIRS/AMSU/HSB on the Aqua mission: Design, science objectives, data
 477 products, and processing systems, *Geoscience and Remote Sensing, IEEE*
 478 *Transactions on*, 41, 253-264, 2003.
- 479 Bayler, G. M., Aune, R., and Raymond, W.: NWP cloud initialization using GOES
 480 sounder data and improved modeling of nonprecipitating clouds, *Monthly weather*
 481 *review*, 128, 3911-3920, 2000.
- 482 Berrocal, V. J., Raftery, A. E., and Gneiting, T.: Combining spatial statistical and
 483 ensemble information in probabilistic weather forecasts, *Monthly Weather Review*,
 484 135, 1386-1402, 2007.
- 485 Blumstein, D., Chalon, G., Carlier, T., Buil, C., Hebert, P., Maciaszek, T., Ponce, G.,
 486 Phulpin, T., Tournier, B., and Simeoni, D.: IASI instrument: Technical overview
 487 and measured performances, *Optical Science and Technology, the SPIE 49th*
 488 *Annual Meeting*, 2004, 196-207,
- 489 Brückner, M., Pospichal, B., Macke, A., and Wendisch, M.: A new multispectral
 490 cloud retrieval method for ship - based solar transmissivity measurements, *Journal*
 491 *of Geophysical Research: Atmospheres*, 119, 2014.
- 492 Descombes, G., Auligne, T., and Lin, H.-C., Xu, D., Schwartz, C. S., Vandenberghe,
 493 F.: Multi-sensor Advection Diffusion nowCast (MADCast) for cloud analysis and
 494 short-term prediction., *NCAR Technical Note NCAR/TN-509+STR*, , 21 pp.,
 495 2014.
- 496 Eyre, J. R., and Menzel, W. P.: Retrieval of cloud parameters from satellite sounder
 497 data: A simulation study, *Journal of Applied Meteorology*, 28, 267-275, 1989.
- 498 Han, Y., Delst, P. V., Liu, Q., Weng, F., Yan, B., Treadon, R., and Derber, J.: JCSDA
 499 Community Radiative Transfer Model (CRTM)—Version 1, *NOAA Tech. Rep.*
 500 *NESDIS*, 122, 33, 2006.
- 501 Hu, M., Xue, M., and Brewster, K.: 3DVAR and Cloud Analysis with WSR-88D
 502 Level-II Data for the Prediction of the Fort Worth, Texas, Tornadic
 503 Thunderstorms. Part I: Cloud Analysis and Its Impact, *Monthly Weather Review*,
 504 134, 675-698, 10.1175/mwr3092.1, 2006.



- 505 Huang, H.-L., Smith, W. L., Li, J., Antonelli, P., Wu, X., Knuteson, R. O., Huang, B.,
 506 and Osborne, B. J.: Minimum local emissivity variance retrieval of cloud altitude
 507 and effective spectral emissivity-simulation and initial verification, *Journal of*
 508 *applied meteorology*, 43, 795-809, 2004.
- 509 Karlsson, K.-G., Johansson, E., and Devasthale, A.: Advancing the uncertainty
 510 characterisation of cloud masking in passive satellite imagery: Probabilistic
 511 formulations for NOAA AVHRR data, *Remote Sensing of Environment*, 158,
 512 126-139, 2015.
- 513 Kleist, D. T., Parrish, D. F., Derber, J. C., Treadon, R., Wu, W. S., and Lord, S.:
 514 Introduction of the GSI into the NCEP Global Data Assimilation System, *Weather*
 515 *and Forecasting*, 24, 1691-1705, 10.1175/2009waf2222201.1, 2009.
- 516 Liu, Q., and Weng, F.: Advanced doubling-adding method for radiative transfer in
 517 planetary atmospheres, *Journal of the atmospheric sciences*, 63, 3459-3465, 2006.
- 518 Mace, G. G., 2004: Level 2 GEOPROF product process description and interface
 519 control document (v.3): Level 2 GEOPROF product process description and
 520 interface control document (v.3), Tech. rep., CIRA, Colorado State University,
 521 2004.
- 522 Menzel, W., Smith, W., and Stewart, T.: Improved cloud motion wind vector and
 523 altitude assignment using VAS, *Journal of Climate and Applied meteorology*, 22,
 524 377-384, 1983.
- 525 Menzel, W. P., and Purdom, J. F.: Introducing GOES-I: The first of a new generation
 526 of geostationary operational environmental satellites, *B Am Meteorol Soc*, 75,
 527 757-781, 1994.
- 528 Platnick, S., King, M. D., Ackerman, S. A., Menzel, W. P., Baum, B. A., Riédi, J. C.,
 529 and Frey, R. A.: The MODIS cloud products: Algorithms and examples from
 530 Terra, *Geoscience and Remote Sensing, IEEE Transactions on*, 41, 459-473, 2003.
- 531 Rossow, W. B., and Schiffer, R. A.: ISCCP cloud data products, *B Am Meteorol Soc*,
 532 72, 2-20, 1991.
- 533 Rossow, W. B., Walker, A. W., and Garder, L. C.: Comparison of ISCCP and other
 534 cloud amounts, *Journal of Climate*, 6, 2394-2418, 1993.
- 535 Shen, Z. Q., and Tang, Y. M.: A modified ensemble Kalman particle filter for
 536 non-Gaussian systems with nonlinear measurement functions, *J Adv Model Earth*
 537 *Sy*, 7, 50-66, 2015.
- 538 Skamarock, W., C, Klemp, J. B., Dudhia, J., Gill, D. O., Barker, D. M., Duda, G.,
 539 Huang, X.-Y., Wang, W., and Powers, J. G.: A description of the Advanced
 540 Research WRF version 3., NCAR, 113, 2008.
- 541 Smith, A., Atkinson, N., Bell, W., and Doherty, A.: An initial assessment of
 542 observations from the Suomi - NPP satellite: data from the Cross - track Infrared
 543 Sounder (CrIS), *Atmospheric Science Letters*, 16, 260-266, 2015.
- 544 Snyder, C., and Zhang, F. Q.: Assimilation of simulated Doppler radar observations
 545 with an ensemble Kalman filter, *Monthly Weather Review*, 131, 1663-1677, Doi
 546 10.1175//2555.1, 2003.
- 547 Snyder, C., Bengtsson, T., Bickel, P., and Anderson, J.: Obstacles to high-dimensional
 548 particle filtering, *Monthly Weather Review*, 136, 4629-4640, 2008.



- 549 Stephens, G. L., Vane, D. G., Boain, R. J., Mace, G. G., Sassen, K., Wang, Z.,
550 Illingworth, A. J., O'Connor, E. J., Rossow, W. B., and Durden, S. L.: The
551 CloudSat mission and the A-Train: A new dimension of space-based observations
552 of clouds and precipitation, *B Am Meteorol Soc*, 83, 1771-1790, 2002.
- 553 van Leeuwen, P. J.: Nonlinear data assimilation in geosciences: an extremely efficient
554 particle filter, *Quarterly Journal of the Royal Meteorological Society*, 136,
555 1991-1999, 2010.
- 556 Wu, W.-S., Purser, R. J., and Parrish, D. F.: Three-dimensional variational analysis
557 with spatially inhomogeneous covariances, *Mon. Wea. Rev.*, 130, 2905-2916,
558 2002.
- 559 Wu, X., and Smith, W. L.: Assimilation of ERBE data with a nonlinear programming
560 technique to improve cloud-cover diagnostics, 120, 2009-2004, 1992.
- 561 Xu, D., Auligné, T., and Huang, X.-Y.: A Retrieval Method for 3-D Cloud Parameters
562 Using Radiance Observations from Multiple Satellites, *Advances in atmospheric
563 physics*, 32, 349-362, 2015.
- 564 Xu, D. M., Liu, Z. Q., Huang, X. Y., Min, J. Z., and Wang, H. L.: Impact of
565 assimilating IASI radiance observations on forecasts of two tropical cyclones (vol
566 122, pg 1, 2013), *Meteorology and Atmospheric Physics*, 122, 227-227,
567 10.1007/s00703-013-0295-z, 2013.
- 568 Zhao, C., Xie, S., Klein, S. A., Protat, A., Shupe, M. D., McFarlane, S. A., Comstock,
569 J. M., Delanoë, J., Deng, M., and Dunn, M.: Toward understanding of differences
570 in current cloud retrievals of ARM ground - based measurements, *Journal of
571 Geophysical Research: Atmospheres*, 117, 2012.

572